

The built-in electric field across FeN/Fe₃N interface for efficient electrochemical reduction of CO₂ to CO

Received: 9 August 2022

Jie Yin^{1,6}✉, Jing Jin^{1,6}, Zhouyang Yin^{2,6}, Liu Zhu^{3,6}, Xin Du⁴✉, Yong Peng³, Pinxian Xi¹✉, Chun-Hua Yan^{1,5} & Shouheng Sun^{1,2}✉

Accepted: 15 March 2023

Published online: 28 March 2023

 Check for updates

Nanostructured metal-nitrides have attracted tremendous interest as a new generation of catalysts for electroreduction of CO₂, but these structures have limited activity and stability in the reduction condition. Herein, we report a method of fabricating FeN/Fe₃N nanoparticles with FeN/Fe₃N interface exposed on the NP surface for efficient electrochemical CO₂ reduction reaction (CO₂RR). The FeN/Fe₃N interface is populated with Fe–N₄ and Fe–N₂ coordination sites respectively that show the desired catalysis synergy to enhance the reduction of CO₂ to CO. The CO Faraday efficiency reaches 98% at −0.4 V vs. reversible hydrogen electrode, and the FE stays stable from −0.4 to −0.9 V during the 100 h electrolysis time period. This FeN/Fe₃N synergy arises from electron transfer from Fe₃N to FeN and the preferred CO₂ adsorption and reduction to *COOH on FeN. Our study demonstrates a reliable interface control strategy to improve catalytic efficiency of the Fe–N structure for CO₂RR.

Converting CO₂ back to carbon (C)-based chemicals/fuels is a critical step en route to realizing green environment and energy sustainability^{1–5}. CO₂ can in principle be reduced to active forms of C-products, but the activated CO₂ intermediates tend to undergo different reaction pathways, making it difficult to efficiently control the reaction selectivity^{6–8}. Recently, the electrochemical CO₂ reduction reaction (CO₂RR) has been studied extensively due to its appealing potential to reduce CO₂ with renewable electricity^{9,10}. The center of these studies lies in the development of robust catalysts to lower the reduction overpotentials and to direct reaction pathways towards specific C-products. Among all possible products generated from the CO₂RR, CO is an important precursor that is widely used for preparing other chemicals and fuels^{11–13}. In the CO₂RR process, CO is produced via two electron reduction of CO₂^{14,15}, and this reaction can be catalyzed by many different catalysts, including not only noble metals (Au, Ag, and Pd)¹⁶, but also non-noble metals (Cu, CuIn alloys)^{17,18}, and metal–N₄

(M–N₄) complex structures^{19–21}, as summarized in Supplementary Table 1. The M–N₄ structures, especially Ni–N- and Fe–N-based structures, have attracted particular interest as a class of catalysts for CO₂RR to CO due to increased electron conductivity with decreased band gap of M–N₄ structures and intensive bonding interactions between *COOH intermediates and metal centers, thus lowering the overall reaction barriers and promoting CO generation. However, the Ni–N-complex catalysis is limited by slow kinetics of CO₂ + H⁺ + e[−] → *COOH and weak *H binding for necessary hydrogenation steps, while the Fe–N-complex catalysis is hindered by the strong *CO and *H binding to the Fe–N sites, which prevent CO from being released as a gas form, or from being further activated for the following hydrogenation steps^{20,22–24}. Therefore, it is important to stabilize the chemical environment of metal–N-catalysts and to optimize their catalysis towards hydrogenation or desorption of CO at low overpotentials for successful CO₂RR.

¹State Key Laboratory of Applied Organic Chemistry, College of Chemistry and Chemical Engineering, Lanzhou University, Lanzhou, China. ²Department of Chemistry, Brown University, Providence, RI, USA. ³Electron Microscopy Centre of Lanzhou University, Lanzhou University, Lanzhou, China. ⁴College of Chemistry, Zhengzhou University, Zhengzhou, China. ⁵State Key Laboratory of Rare Earth Materials Chemistry and Applications, Peking University, Beijing, China. ⁶These authors contributed equally: Jie Yin, Jing Jin, Zhouyang Yin, Liu Zhu. ✉e-mail: yinj@lzu.edu.cn; dux@zzu.edu.cn; xipx@lzu.edu.cn; ssun@brown.edu

Here, we report a strategy to improve Fe–N catalysis efficiency for CO₂RR. The catalyst is based on FeN/Fe₃N heterostructure nanoparticles (NPs) in which Fe is coordinated by 4 N's and 2 N's respectively, forming a unique Fe–N₄/Fe–N₂ interface on the NP surface. This interface offers the desired synergistic effect on CO₂ adsorption on FeN, and electron transfer from Fe₃N to FeN, enhancing the CO₂ reduction to CO. In the CO₂-saturated 0.5 M KHCO₃ solution, the catalyst shows a high CO Faradaic efficiency (FE) of 98% at -0.4 V (vs. RHE) without noticeable efficiency change in the 100 h electrolysis test between -0.4 V and -0.9 V. The catalysis produces CO with a high single-pass conversion rate up to 56%, which is unprecedented. Our study presents an interface design strategy for improving CO₂RR catalysis efficiency.

Results

The FeN/Fe₃N NPs were prepared via nitridation of an Fe salt that was pre-deposited on the commercial Ketjen (KJ) carbon support. In the process, Fe(NO₃)₃·9H₂O urea and carbon support were mixed in water under ultrasonication, separated from the solution, washed with ethanol and deionized (DI) water, and dried under vacuum at 60 °C. The dried sample was then annealed under a flow of ammonia gas at different temperatures (300, 500, and 700 °C) to initiate iron nitride NP formation (see details in methods, and Supplementary Fig. 1). The

NP crystal structure was analyzed by powder X-ray diffraction (XRD). Annealing at 300 °C led to the formation of FeN NPs with a cubic structure (space group F-43m, JCPDS No. 50–8017, $a=b=c=4.307$ Å), annealing at 700 °C gave Fe₃N NPs with a hexagonal structure (space group of P312, JCPDS No. 72–2125, $a=b=4.789$ Å, $c=4.710$ Å), while annealing at 500 °C yielded FeN/Fe₃N NPs (Fig. 1a). The FeN/Fe₃N, FeN, and Fe₃N NPs are spherical and uniform, as shown in the scanning transmission electron microscopy (STEM) image (Fig. 1b and Supplementary Fig. 2). STEM mapping images display the similar Fe and N elements distribution across each FeN/Fe₃N (Fig. 1c), FeN and Fe₃N NP (Supplementary Fig. 2). The high-resolution TEM (HRTEM) image of the FeN/Fe₃N NPs (Fig. 1d) shows clear FeN/Fe₃N domains and interfaces with the lattice mismatch at 5.12% (detail in Methods). The detailed analysis of the FeN/Fe₃N area by high resolution high-angle annular dark field aberration-corrected STEM (HAADF-STEM) reveals that the interface is created by the junction between cubic FeN and hexagonal Fe₃N (Fig. 1e) with obvious atomic dislocation and two distinct diffraction spots at the junction (Supplementary Fig. 3). Away from the junction, the FeN (Supplementary Fig. 4) and Fe₃N (Supplementary Fig. 5) regions are in single crystalline, showing no atomic dislocation. Additionally, the fast Fourier transform (FFT) images (Supplementary Fig. 6) of different regions in Fig. 1e further confirm the FeN/Fe₃N interface is formed with slightly distorted cubic and

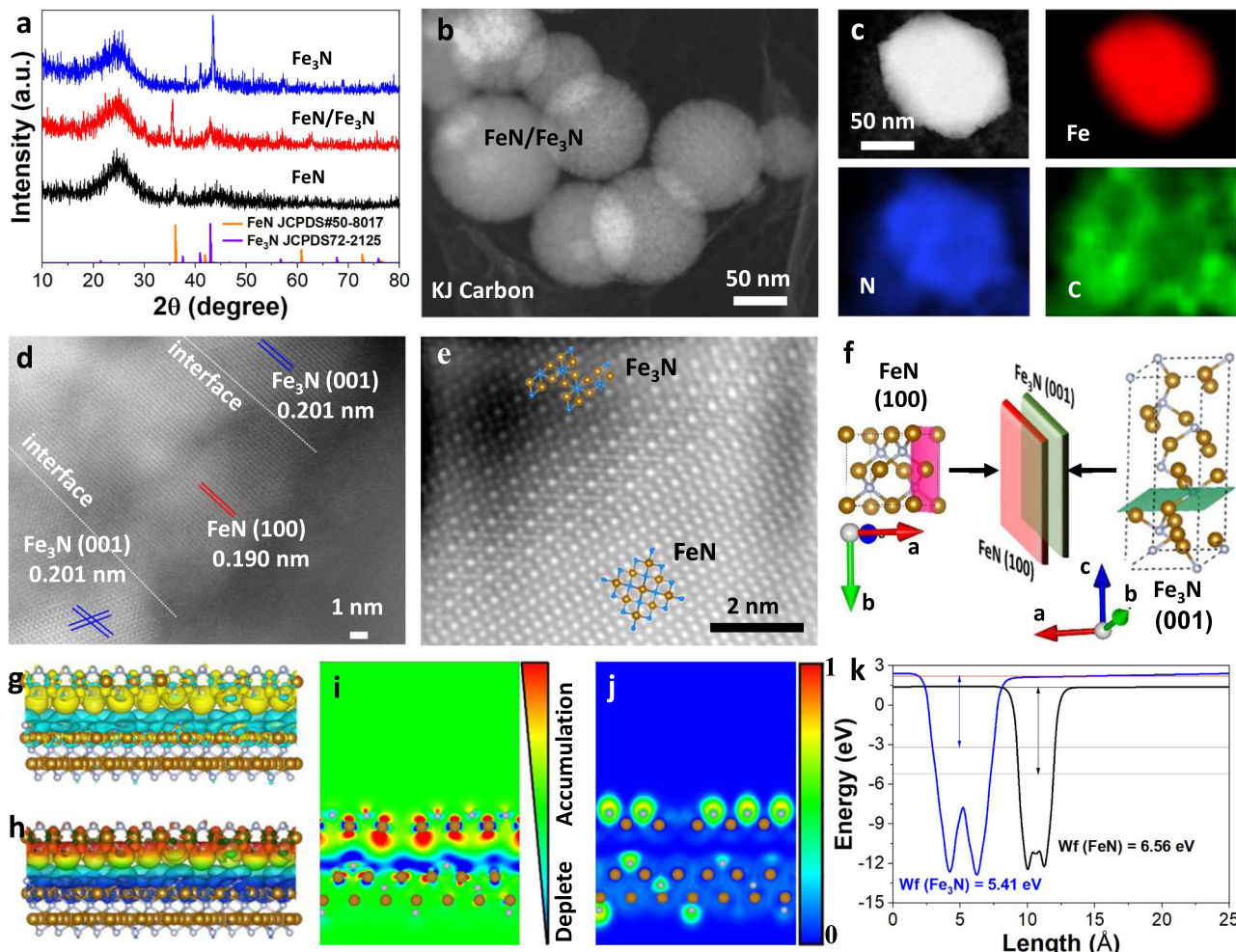


Fig. 1 | Fe-N NP characterization. **a** XRD patterns of FeN, FeN/Fe₃N, and Fe₃N NPs. **b** STEM image of FeN/Fe₃N NPs. **c** Elemental mapping of Fe, N and C of a single FeN/Fe₃N NP. **d** HRTEM image of FeN/Fe₃N NPs showing the interface between FeN and Fe₃N domains. **e** HRHAADF-STEM image of the FeN/Fe₃N interface. **f** Schematic illustration of the FeN/Fe₃N interface formed between FeN (100) and Fe₃N (001). **g** 3D electron density difference distributions at the FeN/Fe₃N interface. **h** The electrostatic potential of the FeN/Fe₃N interface. **i** The electron localization function of the FeN/Fe₃N interface. **j** 2D cross-section of electron density difference at the FeN/Fe₃N interface. **k** The calculated work functions (W_f) of FeN and Fe₃N.

g 3D electron density difference distributions at the FeN/Fe₃N interface. **h** The electrostatic potential of the FeN/Fe₃N interface. **i** The electron localization function of the FeN/Fe₃N interface. **j** 2D cross-section of electron density difference at the FeN/Fe₃N interface. **k** The calculated work functions (W_f) of FeN and Fe₃N.

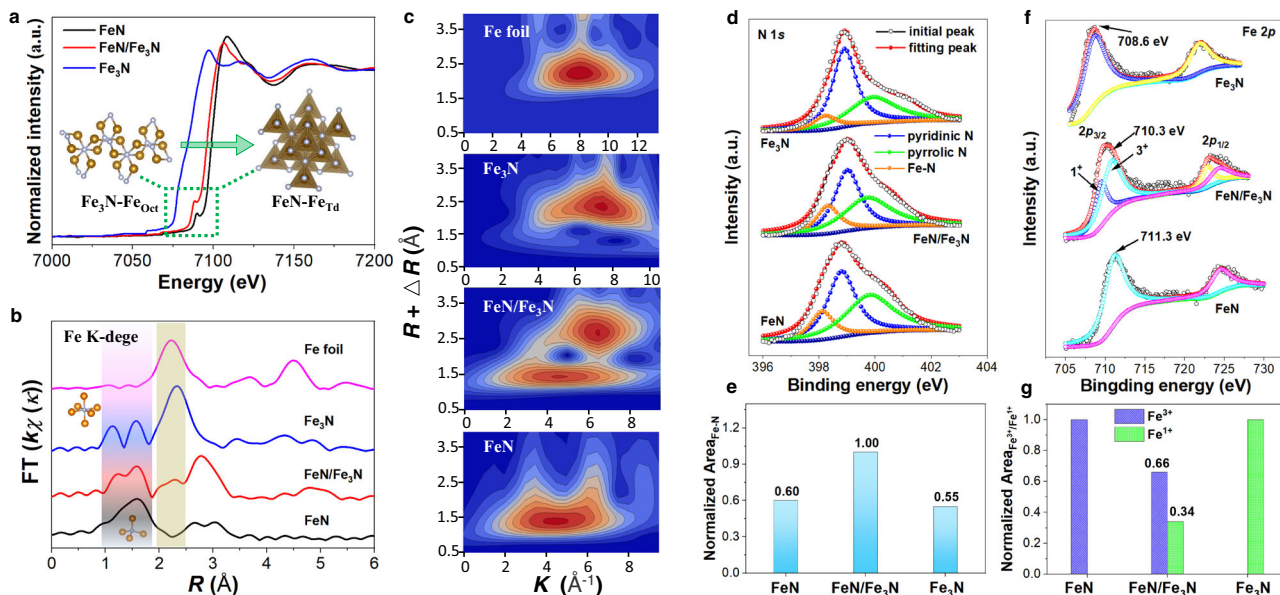


Fig. 2 | Fe-N NP coordination and electron structure characterization. **a** The normalized Fe K-edge EXAFS spectra. Inset: the local FeN structure showing tetrahedral coordination (right) and Fe₃N structure showing octahedral coordination (left). **b** Fe K-edge FT-EXAFS in R space and **c** wavelet transforms for the k³-weighted

EXAFS signals for FeN, FeN/Fe₃N, Fe₃N, and Fe foil. **d** The N 1s XPS spectra, **e** the normalized area of Fe-N bond, **f** the Fe 2p XPS spectra, and **g** the normalized area of Fe³⁺/Fe¹⁺ for FeN, FeN/Fe₃N, and Fe₃N, respectively.

hexagonal structure. The N₂ and CO₂ adsorption ability of the Fe-N structures were measured by the Brunner–Emmet–Teller (BET) method under N₂ and CO₂ atmosphere (Supplementary Fig. 7). The FeN/Fe₃N structure adsorbs more N₂ (736.1 m² g⁻¹) than the FeN (314.5 m² g⁻¹) and Fe₃N (586.0 m² g⁻¹) ones, while the FeN structure adsorbs more CO₂ (25.8 cm² g⁻¹) than the FeN/Fe₃N (24.7 cm² g⁻¹) and Fe₃N (11.2 cm² g⁻¹) ones, suggesting that the FeN/Fe₃N structure may be more porous, but it is the presence of the Fe–N₄ coordination sites in the FeN structure that shows higher CO₂ adsorption power.

We used the density functional theory (DFT) to further investigate the FeN/Fe₃N structure (Fig. 1f–k). The (100) planes of FeN (pink) (interplanar distance 4.230 Å) and (001) planes of Fe₃N (green) (interplanar distance 4.656 Å) match well to form the junction (Fig. 1f). We calculated electron density difference distributions²⁵ between the FeN/Fe₃N interface. As shown in Fig. 1g, the electron clouds around N and Fe in the FeN region (yellow) are much more enriched than that in the Fe₃N region (blue), indicating the electron transfer from Fe₃N to FeN. Due to this electron transfer, the FeN region becomes nucleophilic (Fig. 1h red and yellow region), while the Fe₃N region is electrophilic (Fig. 1h blue region). The distribution of electrons across the interface structure was studied by 2D electron density distribution and electron location function, as shown in Fig. 1i, j. More electrons are localized over the FeN domain than over the Fe₃N one. This is further supported by the calculated electrostatic potential²⁶ (Fig. 1k) with the work function of FeN at 6.56 eV and Fe₃N at 5.41 eV. Therefore, in the FeN/Fe₃N interface structure, there exists a built-in electric field from Fe₃N to FeN.

The Fe K-edge of the extended X-ray absorption fine structure spectroscopy (EXAFS) of the Fe₃N/FeN NPs show the increased energy of the fingerprint peak from Fe₃N (7096.8 eV) to FeN (7108.5 eV) (Fig. 2a), indicating the Fe valence state change from +1 in Fe₃N to +3 in FeN^{27,28}. There is also a fingerprint peak (7106.4 eV) that is located in the middle of the Fe₃N and FeN, implying that the Fe valence in the FeN/Fe₃N interface region is between +1 and +3. The pre-edge peaks at 7089.7 and 7088.2 eV are from Fe–N₄ with tetrahedral coordination (Fe_{Td}, Inset in Fig. 2a right)^{29,30}, not the octahedral coordination (Fe_{Oc}, Inset in Fig. 2a left) in the Fe₃N structure³¹. The Fourier transform k³-weighted EXAFS (FT-EXAFS) spectra in Fig. 2b (R space) show main

peaks in the range from 1 to 3 Å. With more N binding to Fe, the Fe–Fe distance gets longer and longer (in the 2–3 Å range), but the Fe–N distance is shorter (in the 1–2 Å range), showing a double peak for the Fe_{Oc}–N (in the Fe₃N structure) and a broad peak for the Fe_{Td}–N (in the FeN structure). The main peak at 2.33 Å in the Fe₃N spectrum is close to the Fe–Fe bond (2.23 Å) measured from the Fe foil. Fittings of the FeN (Supplementary Fig. 8 and Supplementary Table 2) and Fe₃N (Supplementary Fig. 9 and Supplementary Table 3) spectra suggest that Fe has a coordination number (CN) of 3.92 and 1.40 respectively. The FeN/Fe₃N structure shows more complex peaks in the R-space with Fe–N₄ peak at 1.60 Å and Fe–N₂ peak at 2.33 Å. The corresponding fitting gives the CN of 3.60 for the Fe–N₄ and 1.80 for the Fe–N₂ structure (Supplementary Fig. 10 and Supplementary Table 4). The Fe–N structures were further analyzed by wavelet transform of the EXAFS²⁶. As shown in Fig. 2c, both FeN and FeN/Fe₃N have the K values centered around 4.8 Å⁻¹, while those values from Fe₃N and FeN/Fe₃N locate at 6.5 (FeN/Fe₃N) and 7.5 Å⁻¹ (FeN), closer to 8.2 Å⁻¹ observed from the Fe foil. All these analyses confirm that the Fe₃N structure has more metal character than the FeN structure.

The Fe–N network structure was characterized by Raman spectroscopy (Supplementary Fig. 11). The same D and G peak position with slightly different I_D/I_G values (1.26 for FeN/Fe₃N, 1.15 for FeN, and 1.21 for Fe₃N) suggest that more defects exist in the FeN/Fe₃N structure³², which supports what is concluded from the BET N₂-adsorption analysis. X-ray photoelectron spectroscopy (XPS) shows that the NP sample contains C (C 1s spectra at 284.6 eV, Supplementary Fig. 12) and three different N's (N 1s spectra, Fig. 2d)³³. The FeN/Fe₃N interface structure has the largest Fe–N bonding area (Fig. 2e). Two spin-orbit doublets of Fe 2p can be found in Fe 2p spectra (Fig. 2f). The Fe 2p_{3/2} peaks shift from 711.3 eV (for FeN) to 708.6 eV (for Fe₃N) while the peak for the FeN/Fe₃N interface structure locates at 710.3 eV, indicating that the Fe valence state in the FeN/Fe₃N structure is between FeN and Fe₃N and electrons are drawn from Fe₃N to FeN. Comparing with the normalized Fe–N bonding area for FeN and Fe₃N, we calculated that the FeN/Fe₃N interface structure contained 66% FeN and 34% Fe₃N (Fig. 2g). The Fe binding environment was finally characterized by Mössbauer spectroscopy^{34,35}, as shown in Supplementary Fig. 13. The fitting matches well with the experimental spectra, indicating that the FeN, FeN/

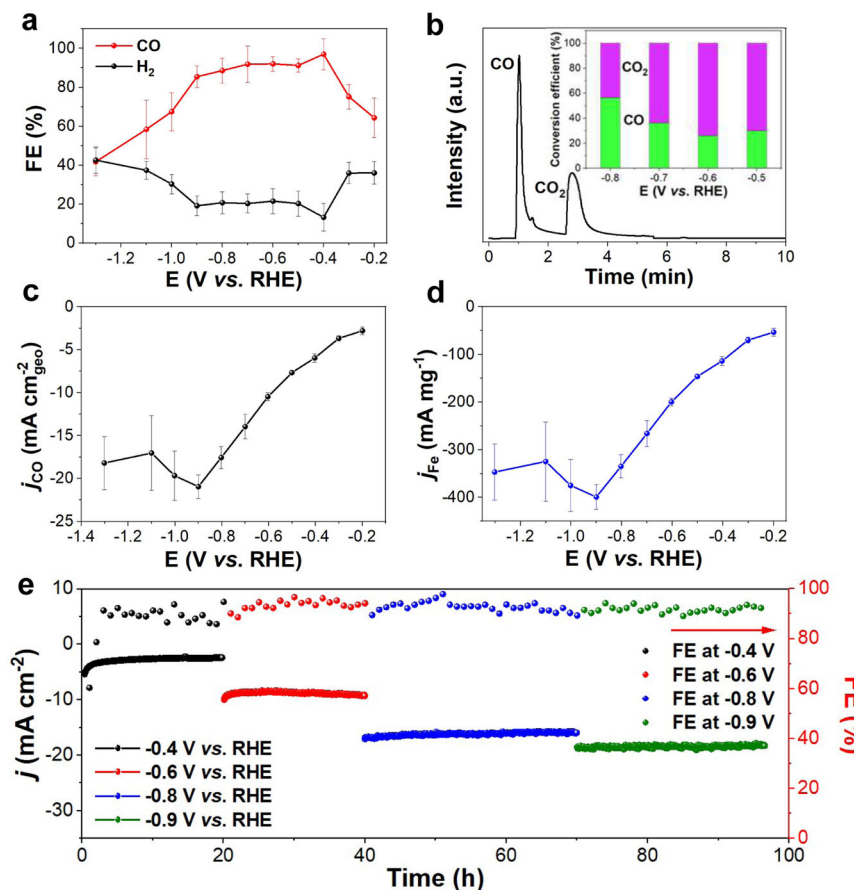


Fig. 3 | CO₂RR performance of the FeN/Fe₃N catalyst. **a** Reduction potential dependent FEs of CO and H₂. **b** GC spectrum of the gas products upon a single pass CO₂ conversion (Inset: reduction potential dependent CO₂ conversion to CO). **c** CO partial current density and **d** corresponding mass activity. **e** CO₂RR current density

and CO FE changes at different reduction potentials over different electrolysis times. Error bars in **a-d** represent the standard deviation of three independent measurements.

Fe₃N, and Fe₃N structures have the Fe–N₄, Fe–N₄/Fe–N₂, and Fe–N₂ coordination, respectively.

The electrocatalytic performance of these Fe–N NP catalysts for CO₂RR was evaluated by linear scan voltammetry (LSV, Supplementary Fig. 14) and cyclic voltammetry (CV, Supplementary Fig. 15) in an H-type cell filled with the Ar- and CO₂-saturated 0.5 M KHCO₃ electrolyte at room temperature^{36,37}. The FeN/Fe₃N structure is more responsive to the voltammetry tests, showing higher current density than either the FeN or Fe₃N structure, suggesting that it initiates more CO₂RR. Under a constant reduction potential, CO₂RR products were characterized by gas chromatograph (GC) and nuclear magnetic resonance (NMR). In the current electrocatalytic reaction condition, the FeN/Fe₃N structure is the most active catalyst for reducing CO₂ to CO with the CO formation FE reaching 98% at -0.4 V and above 90% at -0.5 to -0.9 V (Fig. 3a). The H₂ was another gas product (Supplementary Fig. 16) and no liquid products were detected (Supplementary Fig. 17). The FeN/Fe₃N catalyst shows excellent CO selectivity compared with the recently reported catalysts (Supplementary Table 5). When the reduction potential more negative than -0.9 V, more HER was observed, which was further confirmed by DFT calculations that the H desorption energy was more than 0.9 eV on the FeN/Fe₃N surface (Supplementary Fig. 18). This is also consistent with what was observed previously on ¹H binding energy increase at high potentials on Fe–N-based catalyst surfaces^{24,38}. Based on the GC data from the closed reaction system, the single-pass CO₂ conversion³⁹ reached up to 56% at -0.8 V (Fig. 3b). The FeN/Fe₃N catalyst is much more selective than N doped KJ carbon (CO FE is <20%), FeN (CO FE peaks at ~80% at -0.6 V) and

Fe₃N (CO FE peaks at ~70% at -0.6 V) (Supplementary Fig. 19), which indicates that the FeN/Fe₃N interface structure is key to this CO selectivity enhancement. Its highest CO partial current density is 21 mA cm_{geo}⁻² (Fig. 3c) and the corresponding mass activity is 400 mA mg_{Fe}⁻¹ at -0.9 V, at which its turnover frequency (TOF, Supplementary Fig. 20) is 116 s⁻¹ and turnover number (TON, Supplementary Fig. 20) is 99. The current density data were also normalized by geometric area of working electrode and CO₂-BET area (Supplementary Fig. 21), all of which indicate the high catalytic performance of the FeN/Fe₃N heterostructure. The FeN/Fe₃N catalyst is superior to other representative Au, Ag, and M–N catalysts recently reported for catalyzing CO₂RR to CO (Supplementary Table 5). The stability of the FeN/Fe₃N catalyst was evaluated by time-dependent current change in 0.5 M KHCO₃ at different potentials -0.4, -0.6, -0.8 and -0.9 V (Fig. 3e), which shows negligible decrease in both current density and CO FE in the 100 h testing period. It is worth to note that the CO FE stays above 90% during the tests, which is much better than the stability data obtained from other catalysts previously reported (Supplementary Table 5). We re-evaluated the FeN/Fe₃N structure after the stability test. The XRD pattern (Supplementary Fig. 22a) still shows typical FeN and Fe₃N peaks, the NP morphology is well-maintained in the TEM image (Supplementary Fig. 22b), and the interface structure is intact as evidenced by corresponding auto correlation and FFT images (Supplementary Fig. 22c). The XPS spectra of Fe 2p (Supplementary Fig. 23a) and N 1s (Supplementary Fig. 23b), the EXAFS Fe K-edge spectra of the FeN/Fe₃N (Supplementary Fig. 24a), the pre-edge peak in Fe K-edge (Supplementary Fig. 24a) and FT-EXAFS in R-space

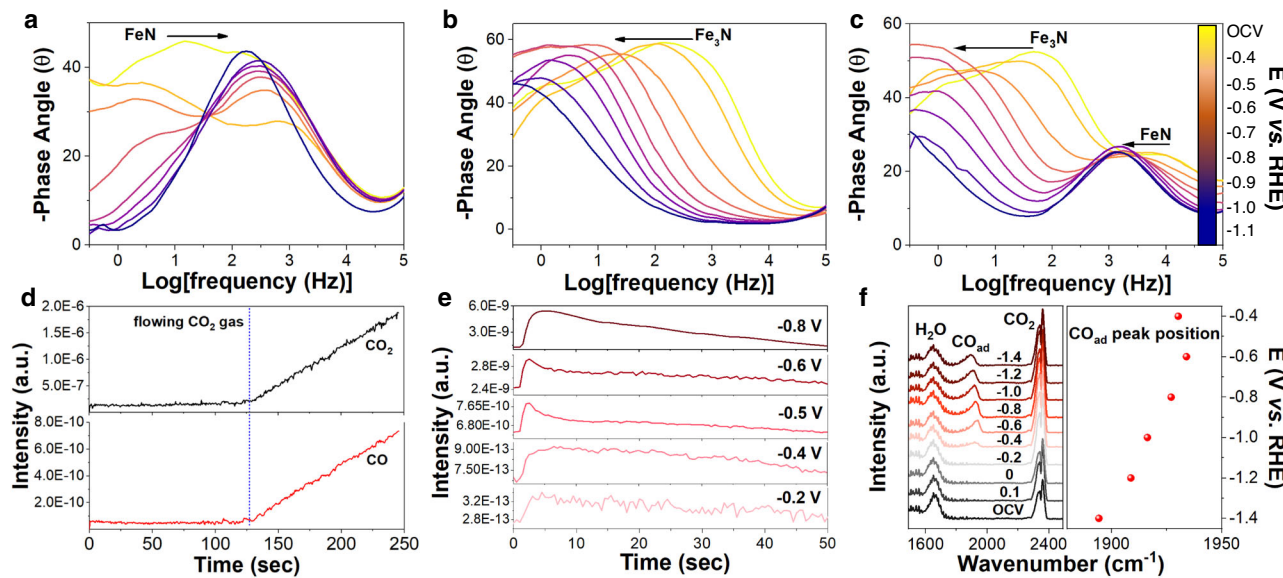


Fig. 4 | In situ spectroscopic studies of Fe-N catalysts and CO₂RR. **a–c** Bode phase plots of FeN **a**, Fe₃N **b**, and FeN/Fe₃N **c** at different reduction potentials. In situ DEMS plots showing the increased presence of CO with increased flowing CO₂

gas **d** and CO signal under different potentials **e** of the FeN/Fe₃N-catalyzed CO₂RR. **f** The in situ SEIR spectra of the FeN/Fe₃N for CO₂RR.

(Supplementary Fig. 24b) all indicate there is no obvious valence state change on Fe in the Fe–N structures, further confirming that the FeN/Fe₃N heterostructure is well-preserved after the stability test.

The evolution of the adsorbed CO₂RR intermediates on Fe–N₄, Fe–N₂, and Fe–N₄/Fe–N₂ sites was studied by in situ electrochemical spectroscopies. The in situ electrochemical impedance spectroscopy (EIS)^{40,41} gives frequency-dependent changes of the Bode phase plots of the Fe–N-coordination sites, which is sensitive to the charge transfer and surface adsorption. The peaks of the FeN structure shift from middle frequency (10⁰–10² Hz) to high-frequency (10²–10⁴ Hz) region (Fig. 4a) due to the low charge transport ability of the Fe–N₄ coordination sites, while those of the Fe₃N structure shift from high-frequency (10²–10⁴ Hz) to middle frequency region (10⁰–10² Hz) (Fig. 4b) due to the poor surface adsorption of CO on the Fe–N₂ coordination sites. In comparison, the FeN/Fe₃N structure shows both FeN- and Fe₃N-type Bode phase peaks, but these peaks shift to lower frequency (Fig. 4c) due to the optimized surface adsorption energy and enhanced charge transport ability from FeN₃ to FeN.

We further conducted in situ differential electrochemical mass spectroscopy (DEMS) test to characterize products separated by the FeN/Fe₃N-catalyzed CO₂RR, from which the concentration of CO increases with the flowing CO₂ gas (Fig. 4d), suggesting the detected CO is due to CO₂RR. The CO signal in DEMS tests is enhanced from -0.2 to -0.8 V vs. RHE (Fig. 4e), indicating that the CO is the main product for CO₂RR (Supplementary Fig. 25). We performed in situ spectra in the CO₂-flowed 0.5 M KHCO₃ electrolyte at various reduction potentials to characterize CO₂ reduction intermediates. The *CO and *H competition was evidenced from in situ surface enhancement infrared spectroscopy (SEIR)^{42,43}. According to the electrochemical Stark effect^{44,45}, the vibrational frequencies of the intermediates adsorbed on an electrode usually shift negatively. As shown in Fig. 4f, there is no peak observed at -1900 cm⁻¹ from open circuit voltage (OCV) to -0.2 V. However, at -0.4 V, a small peak at -1920 cm⁻¹ starts to appear, and shows a negative shift with 49.66 cm⁻¹ per voltage from -0.4 to -1.2 V, which attributes to the adsorbed CO* peak^{46–49}. At more negative potentials, the intensity of the CO peak increases initially, but starts to drop after -1.2 V due to the strong competition of H* generated from the enhanced HER⁵⁰. From the Raman spectra (Supplementary Fig. 26a), the electrolyte, CO₂, CO, and H₂O peaks can be found. The

two peaks for HCO₃⁻ at -1010 cm⁻¹ and CO₃²⁻ at -1060 cm⁻¹ are found from the 0.5 M KHCO₃ electrolyte⁵¹, while the -1920 cm⁻¹ peak has a negative shift from -0.4 to -0.8 V, which corresponds to the stretching vibration mode of the adsorbed CO⁴⁵ (Supplementary Fig. 26b). In situ Raman spectra of CO₂ adsorption peaks at -2330 cm⁻¹ for FeN (Supplementary Fig. 26c), Fe₃N (Supplementary Fig. 26d), and FeN/Fe₃N (Supplementary Fig. 26e) also intensify with enhanced voltage from OCV to -0.8 V vs. RHE (Supplementary Fig. 26f), demonstrating that the FeN/Fe₃N heterostructure has an optimized interfacial adsorption ability.

The formation of CO from CO₂RR is generally believed to follow two proton-coupled electron-transfer steps to form COOH*, and then CO* that is desorbed from the catalyst surface^{52–54}. In this process, the formation of COOH* usually is a potential-limiting step due to the high activation energy of CO₂ molecule. To understand the Fe–N catalysis better, we used DFT to calculate the related activation energy on the catalyst surfaces. We compared the electronic density of states (DOS) and d-band center of Fe₃N, FeN, and FeN/Fe₃N structures^{55–57}. As shown in Fig. 5a, the d-band center of the FeN/Fe₃N heterostructure is at -0.506 eV, while that of FeN is at -0.523 eV and Fe₃N at -0.500 eV, suggesting Fe₃N is beneficial to improve the overall d-band center shift to the Fermi level (E_F). Additionally, the d-band center of pure FeN (100), pure Fe₃N (001), FeN cell, and Fe₃N cell is -0.591, -0.503, -0.647, and -0.502 eV (Supplementary Fig. 27), further demonstrating Fe₃N with rich electron is key for built-in electric field from Fe₃N to FeN. As a result, the intensity of DOS (Supplementary Fig. 28), and the integral DOS (IDOS) (Supplementary Fig. 29) of the FeN/Fe₃N structure is higher than that of the FeN or Fe₃N structure, suggesting that electrons are more populated at E_F level on the FeN/Fe₃N surface for effective binding of reaction intermediates. The FeN/Fe₃N surface potential change upon binding to COOH and CO was calculated by electrostatic potentials and shown as colored contours in Fig. 5b (for *COOH) and Fig. 5c (for *CO), which shows that electron transfer causes a decrease in the potential of CO and COOH (red means lower electrostatic potential and blue means higher electrostatic potential). The corresponding 3D electron density distributions on the FeN/Fe₃N (Fig. 5d, e), FeN (Supplementary Fig. 30c, d), and Fe₃N (Supplementary Fig. 31c, d) surfaces upon their binding to COOH and CO suggest that electrons are transferred from catalyst to COOH/CO. The electron localization of COOH and CO on the FeN, Fe₃N, and FeN/Fe₃N surface

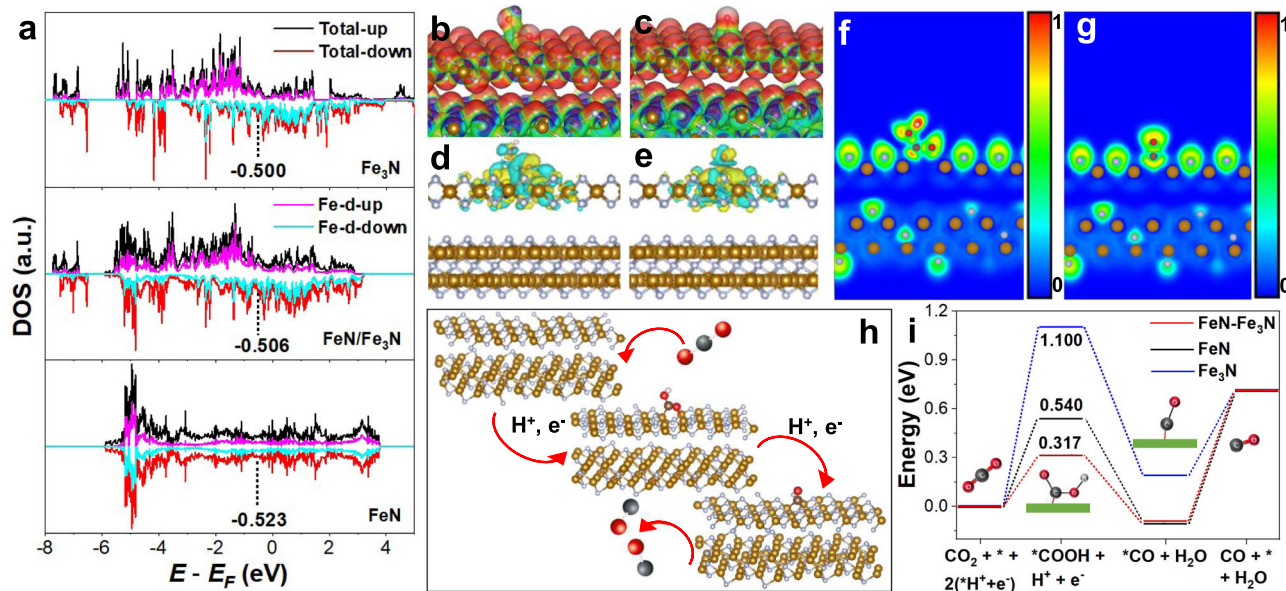


Fig. 5 | DFT calculations on the Fe–N catalyzed CO₂RR. **a** The electronic density of states and d-band centers of Fe in the FeN, Fe₃N, and FeN/Fe₃N structures. The electrostatic potential for adsorption of COOH **b** and CO **c** on the FeN/Fe₃N interface. 3D electron density difference distributions for adsorption of COOH

d and CO **e** on the FeN/Fe₃N interface. The electron localization for adsorption of COOH **f** and CO **g** on the FeN/Fe₃N interface. **h** Schematic reaction CO₂RR to CO pathway projected on the FeN/Fe₃N surface. **i** The calculated Gibbs free energy diagrams for CO₂RR on the FeN, Fe₃N, and FeN/Fe₃N surfaces.

calculated by electron localization function is about 0.8, 0.7, 0.8 (Supplementary Fig. 30e, Supplementary Fig. 31e and Fig. 5f) for COOH and 0.7, 0.7, 0.7 (Supplementary Fig. 30f, Supplementary Fig. 31f and Fig. 5g) for CO, indicating that COOH and CO interact covalently with the catalyst surface^{58–60}. Following the common CO₂RR reaction pathway specifically on the FeN/Fe₃N surface (Fig. 5h), we calculated the Gibbs free energy (ΔG) for the potential-limiting step (CO₂ad to *COOH) on the FeN/Fe₃N structure to be 0.317 eV (Fig. 5i), much lower than that on the FeN (0.540 eV) and Fe₃N (1.10 eV) in the heterostructure. We also calculated the CO₂RR performance on the other side of FeN/Fe₃N heterostructure on the interface Fe₃N (001) (Supplementary Fig. 32a) and other side of Fe₃N (001) (Supplementary Fig. 32b). The ΔG for CO₂ to COOH is 0.985 eV on the interface Fe₃N (001), ΔG for *CO on other side of Fe₃N (001) is −2.566 eV, which is too stable for the CO to dissociate from the plane. ΔG for CO₂ to COOH is about 0.360 and 1.08 eV on the pure FeN (100) (Supplementary Fig. 32c) and pure Fe₃N (001) (Supplementary Fig. 32d), indicating that CO₂ adsorption and activation on the FeN (100) is more favorable for CO₂RR. We further constructed the FeN (110)/Fe₃N (001) heterostructure to reveal the role of the FeN (110) plays on catalyzing CO₂RR. The electron cloud around N and Fe in the Fe₃N region (yellow) is much more enriched than that in the FeN region (blue) (Supplementary Fig. 33a), while is also supported by the 2D electron localization function (Supplementary Fig. 33b). These indicate that the FeN (110)/Fe₃N (001) structure has no electron transport across interface and is not active for CO₂RR. Then, the ΔG for CO₂ad to *COOH on the FeN (110)/Fe₃N (001) structure is 1.189 eV (Supplementary Fig. 33c) much larger than that of FeN (100)/Fe₃N (001) heterostructure, further demonstrating that FeN (100)/Fe₃N (001) heterostructure is superior for CO₂RR. Our calculations support what we concluded from both structure and catalysis analysis of the Fe–N catalysts that the FeN (100)/Fe₃N (001) interface with the built-in electric field has abundant electrons closer to E_F for CO₂ adsorption and activation, showing much enhanced catalysis for CO₂RR to CO.

Discussion

In summary, we have reported a process for synthesizing heterostructured FeN/Fe₃N NPs with the NP surface populated with Fe–N/

Fe–N₂ interfaces. Electron polarization from Fe₃N (Fe–N₂ site) to FeN (Fe–N₄ site) builds the desired electric field across the FeN/Fe₃N interface, enhancing its power to adsorb CO₂. In the electrochemical reduction condition, this FeN/Fe₃N structure has an excellent mass and electron transfer ability in catalyzing CO₂RR to CO with high FE (98% at −0.4 V) and much improved stability in the 100 h electrolysis period (FE > 90% in the broad −0.4 to −0.9 V potential range). The catalyst surface adsorption of CO₂ and its activation intermediates is further characterized by various in situ spectroscopy techniques (EIS, DEMS, IR and Raman) from which the adsorbed CO* is identified. DFT calculations suggest that the FeN/Fe₃N structure has a d-band center that is closer to its E_F level where there are abundant electrons for binding to reaction intermediates (CO₂ad, COOH*, CO*). This strong interaction reduces the ΔG of the CO₂ad to COOH* conversion and provides a necessary force to lower the reduction overpotential and improve the catalytic efficiency. Our work demonstrates that creating a polarized field on the NP surface is a promising approach to the design of highly active catalysts for electrochemical CO₂RR.

Methods

Synthesis of Fe–N based precursor

Firstly, the commercial Ketjen (KJ) carbon (0.1 g) was suspended in water (H₂O, 50 mL) by ultrasound. Then, a mixture of iron (III) nitrate hexahydrate (Fe(NO₃)₃•9H₂O, 0.01 mol, 4.04 g) and urea (CH₄N₂O, 0.1 mol, 6.00 g) was added into the carbon suspension and continued ultrasound for 8 h. Finally, the precipitate was separated by centrifuge (6000 rpm (4830 \times g), 5 min) and washed with water and ethanol for three times and dried under vacuum at 60 °C for 6 h to give the Fe–N based precursor.

Synthesis of FeN, FeN/Fe₃N, and Fe₃N nanosparticles

100 mg Fe–N precursor was placed in crucible and put in the tube furnace (Supplementary Fig. 1). Then the tube was heated to 300, 500 or 700 °C with a rate of 5 °C min^{−1} for 2 h under the flowing NH₃ atmosphere. Finally, the system was cooled to room temperature under a flowing NH₃ gas. In this process, FeN, FeN/Fe₃N and Fe₃N were obtained at 300 °C, 500 °C, and 700 °C, respectively³³.

Catalyst characterization

X-ray diffraction (XRD) experiments were conducted from 20° to 90° on an X'Pert ProX-ray diffractometer with Cu Ka radiation ($\lambda = 0.1542$ nm) under a voltage of 40 kV and a current of 40 mA. Sample compositions were determined by ICP-AES (HITACHI P-4010, Japan). Product morphology was imaged by field-emission scanning electron microscopy (FESEM, Zeiss) at an acceleration voltage of 5 kV. All samples were coated with a thin layer of gold prior to FESEM observations. More detailed product morphology and structure were analyzed by transmission electron microscopy (TEM) and high-resolution transmission electron microscopy (HRTEM) under an acceleration voltage of 200 kV with a JEOL JEM 2100 TEM. Atomic-scale STEM images were recorded on a probe aberration-corrected STEM (Cubed Titan G2 60-300, FEI, USA) operated at 300 kV. Product surface composition was analyzed by X-ray photoelectron spectroscopy (XPS) with a VG ESCALAB 220i-XL device. All XPS spectra were corrected using C1s line at 284.6 eV. The absorption spectra of Fe K-edge were collected in transmission mode using a Si (111) double-crystal monochromator at the BLW141 station of the Beijing Synchrotron Radiation Facility (BSRF). Transmission ^{57}Fe Mössbauer spectra were recorded by using a conventional spectrometer working in constant acceleration mode. A 50 mCi of ^{57}Co embedded in a Rh matrix moving at room temperature was used as the γ -ray source. The absorber was prepared with a surface density of ~8 mg cm⁻² natural iron. The drive velocity was calibrated with sodium nitroprusside at room temperature and all the isomer shifts quoted in this work are relative to that of the α -Fe.

Lattice mismatch calculation

The lattice mismatch for the heterostructure can be calculated by lattice of different domains, as shown below:

$$\delta = (2 \times |a_1 - a_2|) / (a_1 + a_2) \quad (1)$$

where δ is lattice mismatch, a_1 and a_2 are the lattice parameters of different domains. We define that two lattices are well-matched when δ is <5%, semi-matched if δ is between 5% and 25%, and totally mismatched if δ is >25%. The δ value for the FeN/Fe₃N heterostructure is 5.12% ($\delta_{\text{FeN/Fe}_3\text{N}} = (2 \times |a_{\text{FeN}} - a_{\text{Fe}_3\text{N}}|) / (a_{\text{FeN}} + a_{\text{Fe}_3\text{N}}) = (2 \times |0.19 - 0.20|) / (0.19 + 0.20) = 5.12\%$), therefore, the FeN and Fe₃N lattices are well-matched, which is favorable for electron transfer at the interface.

Electrochemical test for CO₂RR

Electrochemical measurements were carried out at room temperature using the three-electrode system directly connected to a CHI 760 E Electrochemical Workstation (CHI Instruments, Shanghai Chenhua Instrument Corp., China). The CHI workstation was used to conduct CO₂ reduction experiments in aqueous 0.5 M KHCO₃ (pH = 6.8 when saturated with CO₂, pH = 8.3 when saturated with Ar). A platinum wire was used as counter electrode. All potentials were measured against an Ag/AgCl reference electrode (4.0 M KCl, Pine instrument) and were calibrated against a reversible hydrogen electrode (RHE). The experiments were performed in a gas-tight cell with two compartments separated by an anion exchange membrane (Nafion® 212). Each compartment contained 10 mL electrolyte with approximately 10 mL headspace^{6,37}.

Product analysis

CO₂ gas was delivered at an average rate of 30 mL min⁻¹ (at room temperature and ambient pressure) and routed directly into the gas sampling loop of a gas chromatograph (Agilent 7890 A). The gas phase composition was analyzed by GC every 30 min. The GC analysis was set up to split the gas sample into two aliquots whereof one aliquot was routed through a packed MoleSieve 5 A column and a packed HP-PLOT

Q column before passing a thermal conductivity detector (TCD) for H₂ quantification. Argon (Corp Brother, 99.9999%) and Helium (Corp Brother, 99.9999%) were employed as carrier or make-up gases respectively. The second aliquot was routed through a packed HP-PLOT Q + PT column equipped with a flame ionization detector (FID) for analyzing CO and C₁ to C₃ hydrocarbons. The GC was calibrated using commercially available calibration standards from JJS Technical Services. ¹H-NMR spectroscopy was employed to characterize and quantify CO₂ reduction products at the end of the experiments. ¹H-NMR spectra were recorded on Bruker DRX 400/600 Avance. A total of 0.5 mL electrolyte and 0.1 mL D₂O (content 0.05 μ L dimethyl sulfoxide (DMSO), as inner standard) were mixed together to get the NMR signal.

Theoretical calculations

The first-principles density functional theory (DFT) calculations were performed within the generalized gradient approximation (GGA) based on via Vienna ab initio simulation package (VASP)⁶¹⁻⁶³. We constructed FeN/Fe₃N interface structure, FeN and Fe₃N surface model with periodicity in the x and y directions and the depth of the vacuum layer is greater than 20 Å in order to prevent self-interactions. In addition, the bottom two stoichiometric layers were need to be fixed while the top layer and adsorbates (CO*, COOH*) were allowed to relax in the optimization of the FeN/Fe₃N and Fe₃N, for FeN, only one stoichiometric layer needs to be fixed. The VASP was employed to perform all DFT calculations within the functional as proposed by Perdew-Burke-Ernzerh (PBE)^{61,64} of interactions is represented using the projector augmented wave (PAW)^{61,65,66} potential. The Kohn-Sham one-electron valence states were expanded on the basis of plane waves with a cutoff energy of 400 eV in the in the process of structure optimization. A geometry optimization was considered convergent when the electronic energy and Hellmann-Feynman forces convergence criterion was smaller than 10⁻⁵ eV and 0.03 eV Å⁻¹, respectively. The K-point of 3 × 1 × 1 was used for the optimization of the FeN/Fe₃N, FeN and Fe₃N surface, and the corresponding adsorption structure (CO*, COOH*). Subsequently, we calculated the charge density, electron localization function (ELF), work function and electrostatic potential in the self-consistent process. The electronic energy was considered self-consistent while the energy variation was smaller than 10⁻⁵ eV. The value of K-point, cutoff energy is the same as the process of structure optimization. After the self-consistent calculation converges, the charge density distribution, electron localization, electrostatic potential and work function can be obtained, the self-consistent structure is used as the input file, and the wave function and charge density file are read to obtain the density of states of the heterojunction, FeN and Fe₃N.

The d-band center was used to understand the adsorption capacity of the different catalyst (FeN/Fe₃N, FeN and Fe₃N) surface for CO₂. The calculation formula of d-band center:

$$\varepsilon_d = \frac{\int_{-\infty}^{\infty} n_d(\varepsilon) \varepsilon d\varepsilon}{\int_{-\infty}^{\infty} n_d(\varepsilon) d\varepsilon} \quad (2)$$

where $n_d(\varepsilon)$ represents the density of states and ε represents the energy of state.

The Gibbs free energy also was calculated in this study. The zero-point energy (ZPE) correction was performed referring to the approaches previously reported. In the DFT process, we calculated the Gibbs free energy according to the equations as follow⁶¹:

$$G^0 = E_{DFT} + ZPE - TS^0 \quad (3)$$

Where G^0 is the Gibbs free energy, E_{DFT} is total free energy, ZPE is the vibration energy; TS^0 is the entropy change ($T = 298.15$ K).

TOF and TON calculation for FeN/Fe₃N catalyst

The turnover frequency (TOF) was calculated by the following formula:⁶⁷

$$\text{TOF} = \frac{j \times S \times \text{FE}}{2 \times n \times F} \quad (4)$$

where j (mA cm⁻²) is the current density at -0.4 V, S is the surface area of the working electrode, FE is the Faraday efficiency of CO, the number 2 means 2 electrons mol⁻¹ of CO, F is Faraday's constant (96485.3 C mol⁻¹), and n is the moles of coated Fe atoms on the electrode. The Fe content of catalysts was measured by the ICP-AES measurement.

Similarly, the turnover number (TON) of the catalyst was calculated based on:

$$\text{TON} = \text{TOF} \times \text{FE} \times 0.01 \quad (5)$$

Data availability

All data supporting the findings of this study are available in the article and its Supplementary Information. Source data for the following figures are provided with this paper. Figure 1a, k, Fig. 2a–g, Fig. 3a–e, Fig. 4a–f, Fig. 5a, i, Fig. S7a–f, Fig. S8a and b, Fig. S9a and b, Fig. S10a and b, Fig. S11, Fig. S12, Fig. S13a–c, Fig. S14, Fig. S15a and b, Fig. S16, Fig. S17, Fig. S18, Fig. S19a–c, Fig. S20, Fig. S21a and b, Fig. S22a, Fig. S23a, b, Fig. S24a, b, Fig. S25, Fig. S26a–f, Fig. S27a–d, Fig. S28, Fig. S29, Fig. S32a–d, Fig. S33c. Source data are provided with this paper.

References

1. Ren, S. et al. Molecular electrocatalysts can mediate fast, selective CO₂ reduction in a flow cell. *Science* **365**, 367–369 (2019).
2. Turner, J. A. A realizable renewable energy future. *Science* **285**, 687–689 (1999).
3. Wang, X. et al. Regulation of coordination number over single Co sites: triggering the efficient electroreduction of CO₂. *Angew. Chem. Int. Ed.* **57**, 1944–1948 (2018).
4. Ye, K. et al. In situ reconstruction of a hierarchical Sn-Cu/SnO_x core/shell catalyst for high-performance CO₂ electroreduction. *Angew. Chem. Int. Ed.* **59**, 4814–4821 (2020).
5. Wang, J., Tan, H.-Y., Zhu, Y., Chu, H. & Chen, H. M. Linking the dynamic chemical state of catalysts with the product profile of electrocatalytic CO₂ reduction. *Angew. Chem. Int. Ed.* **60**, 17254–17267 (2021).
6. Yin, Z. et al. Cu₃N nanocubes for selective electrochemical reduction of CO₂ to ethylene. *Nano Lett.* **19**, 8658–8663 (2019).
7. Li, X. et al. Exclusive Ni-N₄ sites realize near-unity CO selectivity for electrochemical CO₂ reduction. *J. Am. Chem. Soc.* **139**, 14889–14892 (2017).
8. Artz, J. et al. Sustainable conversion of carbon dioxide: an integrated review of catalysis and life cycle assessment. *Chem. Rev.* **118**, 434–504 (2018).
9. Liu, S. et al. Efficient electrochemical reduction of CO₂ to HCOOH over Sub-2 nm SnO₂ quantum wires with exposed grain boundaries. *Angew. Chem. Int. Ed.* **58**, 8499–8503 (2019).
10. Li, J. et al. Atomically dispersed manganese catalysts for oxygen reduction in proton-exchange membrane fuel cells. *Nat. Catal.* **1**, 935–945 (2018).
11. Geng, Z. et al. Oxygen vacancies in ZnO nanosheets enhance CO₂ electrochemical reduction to CO. *Angew. Chem. Int. Ed.* **57**, 6054–6059 (2018).
12. Shi, R. et al. Efficient wettability-controlled electroreduction of CO₂ to CO at Au/C interfaces. *Nat. Commun.* **11**, 3028 (2020).
13. Su, X., Yang, X.-F., Huang, Y., Liu, B. & Zhang, T. Single-atom catalysis toward efficient CO₂ conversion to CO and formate products. *Acc. Chem. Res.* **52**, 656–664 (2019).
14. Tomboc, G. M., Choi, S., Kwon, T., Hwang, Y. J. & Lee, K. Potential link between Cu surface and selective CO₂ electroreduction: perspective on future electrocatalyst designs. *Adv. Mater.* **32**, 1908398 (2020).
15. Sun, L., Reddu, V., Fisher, A. C. & Wang, X. Electrocatalytic reduction of carbon dioxide: opportunities with heterogeneous molecular catalysts. *Energy Environ. Sci.* **13**, 374–403 (2020).
16. Möller, T. et al. Efficient CO₂ to CO electrolysis on solid Ni-N-C catalysts at industrial current densities. *Energy Environ. Sci.* **12**, 640–647 (2019).
17. Li, Q. et al. Tuning Sn-catalysis for electrochemical reduction of CO₂ to CO via the Core/Shell Cu/SnO₂ structure. *J. Am. Chem. Soc.* **139**, 4290–4293 (2017).
18. Rasul, S. et al. A highly selective copper-indium bimetallic electrocatalyst for the electrochemical reduction of aqueous CO₂ to CO. *Angew. Chem. Int. Ed.* **54**, 2146–2150 (2015).
19. Guo, W. et al. Atomic indium catalysts for switching CO₂ electroreduction products from formate to CO. *J. Am. Chem. Soc.* **143**, 6877–6885 (2021).
20. Ren, W. et al. Isolated diatomic Ni-Fe metal–nitrogen sites for synergistic electroreduction of CO₂. *Angew. Chem. Int. Ed.* **58**, 6972–6976 (2019).
21. Gu, J., Hsu, C.-S., Bai, L., Chen, H. M. & Hu, X. Atomically dispersed Fe³⁺ sites catalyze efficient CO₂ electroreduction to CO. *Science* **364**, 1091–1094 (2019).
22. Yang, H. B. et al. Atomically dispersed Ni(i) as the active site for electrochemical CO₂ reduction. *Nat. Energy* **3**, 140–147 (2018).
23. Kumar, B. et al. Renewable and metal-free carbon nanofibre catalysts for carbon dioxide reduction. *Nat. Commun.* **4**, 2819 (2013).
24. Liang, S., Huang, L., Gao, Y., Wang, Q. & Liu, B. Electrochemical reduction of CO₂ to CO over transition metal/N-doped carbon catalysts: the active sites and reaction mechanism. *Adv. Sci.* **8**, 2102886 (2021).
25. Zhang, S. et al. Solid frustrated-Lewis-pair catalysts constructed by regulations on surface defects of porous nanorods of CeO₂. *Nat. Commun.* **8**, 15266 (2017).
26. Xu, W., Tian, W., Meng, L., Cao, F. & Li, L. Interfacial chemical bond-modulated Z-scheme charge transfer for efficient photoelectrochemical water splitting. *Adv. Energy Mater.* **11**, 2003500 (2021).
27. Adli, N. M. et al. Engineering atomically dispersed FeN₄ active sites for CO₂ electroreduction. *Angew. Chem. Int. Ed.* **60**, 1022–1032 (2021).
28. Yin, J. et al. NiCo₂O₄-based nanosheets with uniform 4 nm mesopores for excellent Zn-Air battery performance. *Adv. Mater.* **32**, 2001651 (2020).
29. Yang, H. B. et al. Atomically dispersed Ni (I) as the active site for electrochemical CO₂ reduction. *Nat. Energy* **3**, 140–147 (2018).
30. Wang, P. et al. Atomically dispersed cobalt catalyst anchored on nitrogen-doped carbon nanosheets for lithium-oxygen batteries. *Nat. Commun.* **11**, 1576 (2020).
31. Ni, B. et al. Optimized enhancement effect of sulfur in Fe–N–S codoped carbon nanosheets for efficient oxygen reduction reaction. *ACS Appl. Mater. Interfaces* **12**, 23995–24006 (2020).
32. Lai, Q. et al. Optimal configuration of N-doped carbon defects in 2D turbostratic carbon nanomesh for advanced oxygen reduction electrocatalysis. *Angew. Chem. Int. Ed.* **59**, 11999–12006 (2020).
33. Yin, J. et al. Ni–C–N nanosheets as catalyst for hydrogen evolution reaction. *J. Am. Chem. Soc.* **138**, 14546–14549 (2016).
34. Li, J. et al. Identification of durable and non-durable FeN_x sites in Fe–N–C materials for proton exchange membrane fuel cells. *Nat. Catal.* **4**, 10–19 (2021).

35. Wang, X.-T. et al. Redox-inert Fe^{3+} ions in octahedral sites of Co-Fe spinel oxides with enhanced oxygen catalytic activity for rechargeable zinc-air batteries. *Angew. Chem. Int. Ed.* **58**, 13291–13296 (2019).

36. Fu, J. et al. Bipyridine-assisted assembly of Au nanoparticles on Cu nanowires to enhance the electrochemical reduction of CO_2 . *Angew. Chem. Int. Ed.* **58**, 14100–14103 (2019).

37. Yin, J. et al. A new hexagonal cobalt nanosheet catalyst for selective CO_2 conversion to ethanal. *J. Am. Chem. Soc.* **143**, 15335–15343 (2021).

38. Ju, W. et al. Understanding activity and selectivity of metal-nitrogen-doped carbon catalysts for electrochemical reduction of CO_2 . *Nat. Commun.* **8**, 944 (2017).

39. Ripatti, D. S., Veltman, T. R. & Kanan, M. W. Charging up stationary energy storage. *Joule* **3**, 1–17 (2019).

40. Xiao, Z. J. et al. Operando identification of the dynamic behavior of oxygen vacancy-rich Co_3O_4 for oxygen evolution reaction. *J. Am. Chem. Soc.* **142**, 12087–12095 (2020).

41. Doyle, R. & Lyons, M. Kinetics and mechanistic aspects of the oxygen evolution reaction at hydrous iron oxide films in base. *J. Electrochem. Soc.* **160**, H142–H154 (2013).

42. Niu, Z.-Z. et al. Hierarchical copper with inherent hydrophobicity mitigates electrode flooding for high-rate CO_2 electroreduction to multicarbon products. *J. Am. Chem. Soc.* **143**, 8011–8021 (2021).

43. Jiang, K. et al. Metal ion cycling of Cu foil for selective C–C coupling in electrochemical CO_2 reduction. *Nat. Catal.* **1**, 111–119 (2018).

44. Chernyshovaa, V. I., Somasundarana, P. & Ponnurangam, S. On the origin of the elusive first intermediate of CO_2 electroreduction. *Proc. Natl Acad. Sci. USA* **115**, E9261–E9270 (2018).

45. Li, F. et al. Cooperative CO_2 -to-ethanol conversion via enriched intermediates at molecule–metal catalyst interfaces. *Nat. Catal.* **3**, 75–82 (2020).

46. Heyes, J., Dunwell, M. & Xu, B. CO_2 reduction on Cu at low overpotentials with surface-enhanced in situ spectroscopy. *J. Phys. Chem. C* **120**, 17334–17341 (2016).

47. Wuttig, A. et al. Tracking a common surface-bound intermediate during CO_2 -to-fuels catalysis. *ACS Cent. Sci.* **2**, 522–528 (2016).

48. Moradzaman, M. & Mul, G. Infrared analysis of interfacial phenomena during electrochemical reduction of CO_2 over polycrystalline copper electrodes. *ACS Catal.* **10**, 8049–8057 (2020).

49. Yang, F., Ma, X., Cai, W.-B., Song, P. & Xu, W. Nature of oxygen-containing groups on carbon for high-efficiency electrocatalytic CO_2 reduction reaction. *J. Am. Chem. Soc.* **141**, 20451–20459 (2019).

50. Gao, J. et al. Selective C–C coupling in carbon dioxide electroreduction via efficient spillover of intermediates as supported by operando Raman spectroscopy. *J. Am. Chem. Soc.* **141**, 18704–18714 (2019).

51. Zhao, Y. et al. Industrial-current-density CO_2 -to- C_2 electroreduction by anti-swelling anion-exchange ionomer-modified oxide-derived Cu nanosheets. *J. Am. Chem. Soc.* **144**, 10446–10454 (2022).

52. Wu, J. et al. Incorporation of nitrogen defects for efficient reduction of CO_2 via two-electron pathway on three-dimensional graphene foam. *Nano Lett.* **16**, 466–470 (2016).

53. Phuc, T. V., Kang, S. G., Chung, J. S. & Hur, S. H. Highly selective metal-organic framework-based electrocatalyst for the electrochemical reduction of CO_2 to CO. *Mater. Res. Bull.* **138**, 111228 (2021).

54. Zhu, Y. et al. Carbon-supported single metal site catalysts for electrochemical CO_2 reduction to CO and beyond. *Small* **17**, 2005148 (2021).

55. Shi, X. et al. A partial sulfuration strategy derived multi-yolk–shell structure for ultra-stable K/Na/Li-ion storage. *Adv. Mater.* **32**, 2100837 (2021).

56. Li, Y. et al. Coupling porous Ni doped LaFeO_3 nanoparticles with amorphous FeOOH nanosheets yields an interfacial electrocatalyst for electrocatalytic oxygen evolution. *J. Mater. Chem. A* **9**, 23545–23554 (2021).

57. Hammer, B. Nørskov, J. K. Theoretical Surface Science and Catalysis-Calculations and Concepts, *Advances In Catalysis*, Volume 45.

58. Zhang, H., Li, Y., Hou, J., Tu, K. & Chen, Z. FeB_6 monolayers: the graphene-like material with hypercoordinate transition metal. *J. Am. Chem. Soc.* **138**, 5644–5651 (2016).

59. Huang, Z.-Q. et al. Understanding all-solid frustrated-Lewis-pair sites on CeO_2 from theoretical perspectives. *ACS Catal.* **8**, 546–554 (2018).

60. Tang, Y., Zhao, S., Long, B., Liu, J.-C. & Li, J. On the nature of support effects of metal dioxides MO_2 ($\text{M} = \text{Ti}, \text{Zr}, \text{Hf}, \text{Ce}, \text{Th}$) in single-atom gold catalysts: importance of quantum primogenic effect. *J. Phys. Chem. C* **120**, 17514–17526 (2016).

61. Kresse, G. & Furthmüller, J. Efficiency of ab-initio total energy calculations for metals and semiconductors using a plane-wave basis set. *Comp. Murer. Sci.* **6**, 15–50 (1996).

62. Kresse, G. & Furthmüller, J. Efficient iterative schemes for ab initio total-energy calculations using a plane-wave basis set. *Phys. Rev. B* **54**, 11169 (1996).

63. Li, W. et al. Promoting body carriers migration of CdS nanocatalyst by N-doping for improved hydrogen production under simulated sunlight irradiation. *Appl. Catal. B: Environ.* **313**, 121470 (2022).

64. Perdew, J. P., Burke, K. & Ernzerhof, M. Generalized gradient approximation made simple. *Phys. Rev. Lett.* **77**, 3865 (1996).

65. Kresse, G. & Joubert, D. From ultrasoft pseudopotentials to the projector augmented-wave method. *Phys. Rev. B* **59**, 1758 (1999).

66. Engel, M., Marsman, M., Franchini, C. & Kresse, G. Electron-phonon interactions using the projector augmented-wave method and Wannier functions. *Phys. Rev. B* **101**, 184302 (2020).

67. Yin, J. et al. NiO/CoN porous nanowires as efficient bifunctional catalysts for Zn–Air batteries. *ACS Nano* **11**, 2275–2283 (2017).

Acknowledgements

This work was funded by the National Key R&D Program of China (2021YFA1501101), the National Natural Science Foundation of China (NSFC) (Nos. 22221001, 22201115, 21931001, and 21922105), the Special Fund Project of Guiding Scientific and Technological Innovation Development of Gansu Province (2019ZX-04), and the 111 Project (B20027), as well as by the Fundamental Research Funds for the Central Universities (Izujbky-2021-pd04, Izujbky-2021-sp41 and Izujbky-2021-it12). The computational resource was supported by National Supercomputing Center in Zhengzhou and (Le Ma) Technical Department, Beijing Zijinggaoke Science and Technology Ltd, and the VASP copyright reserved by echnical Department, Beijing Zijinggaoke Science and Technology Ltd. J.Y. acknowledges the support Natural Science Foundation of Gansu Providence (22JR5RA540) and Gansu Province Youth Science and Technology Talent Promotion Project (GXH202220530-02).

Author contributions

S.S., J.Y., and P.X. designed and led the studies. J.Y. and X.D. led computational project in this work. J.Y., J.J., and Z.Y. synthesized the catalysts and performed the NP characterization and CO2RR. J.J. and J.Y. analyzed the EXAFS and XPS data of the NPs. L.Z., J.J., and Y.P. helped to acquire TEM and HAADF-STEM of the NPs. S.S., P.X., J.Y., Z.Y., J.J., L.Z., X.D., and C.Y. discussed the catalytic process. All authors contributed to the preparation of the manuscript. All authors discussed the results and commented on the manuscript during revisions.

Competing interests

The authors declare no competing interests.

Additional information

Supplementary information The online version contains supplementary material available at <https://doi.org/10.1038/s41467-023-37360-9>.

Correspondence and requests for materials should be addressed to Jie Yin, Xin Du, Pinxian Xi or Shouheng Sun.

Peer review information *Nature Communications* thanks the other anonymous reviewer(s) for their contribution to the peer review of this work.

Reprints and permissions information is available at <http://www.nature.com/reprints>

Publisher's note Springer Nature remains neutral with regard to jurisdictional claims in published maps and institutional affiliations.

Open Access This article is licensed under a Creative Commons Attribution 4.0 International License, which permits use, sharing, adaptation, distribution and reproduction in any medium or format, as long as you give appropriate credit to the original author(s) and the source, provide a link to the Creative Commons license, and indicate if changes were made. The images or other third party material in this article are included in the article's Creative Commons license, unless indicated otherwise in a credit line to the material. If material is not included in the article's Creative Commons license and your intended use is not permitted by statutory regulation or exceeds the permitted use, you will need to obtain permission directly from the copyright holder. To view a copy of this license, visit <http://creativecommons.org/licenses/by/4.0/>.

© The Author(s) 2023